J. Fluid Mech. (2012), *vol.* 693, *pp.* 297–318.
doi:10.1017/jfm.2011.531

Effects of viscoelasticity in the high Reynolds number cylinder wake

David Richter, Gianluca Iaccarino and Eric S. G. Shaqfeh†

Department of Mechanical Engineering, Stanford University, CA 94305, USA

(Received 26 May 2011; revised 17 October 2011; accepted 29 November 2011; first published online 16 January 2012)

At $Re = 3900$, Newtonian flow past a circular cylinder exhibits a wake and detached shear layers which have transitioned to turbulence. It is the goal of the present study to investigate the effects which viscoelasticity has on this state and to identify the mechanisms responsible for wake stabilization. It is found through numerical simulations (employing the FENE-P rheological model) that viscoelasticity greatly reduces the amount of turbulence in the wake, reverting it back to a state which qualitatively appears similar to the Newtonian mode B instability which occurs at lower Re. By focusing on the separated shear layers, it is found that viscoelasticity suppresses the formation of the Kelvin–Helmholtz instability which dominates for Newtonian flows, consistent with previous studies of viscoelastic free shear layers. Through this shear layer stabilization, the viscoelastic far wake is then subject to the same instability mechanisms which dominate for Newtonian flows, but at far lower Reynolds numbers.

Key words: instability, viscoelasticity, wakes

1. Introduction

In Newtonian flow past a circular cylinder, transition to turbulence occurs in several distinct stages as the Reynolds number is increased, and this path of transition is outlined nicely by Williamson (1996*b*). From the two-dimensional, vortex-shedding wake, three-dimensional instabilities begin to form around $Re \approx 190$ through a secondary instability known as the mode A instability. At a Reynolds number of approximately 260, this mode A instability gives way to a second type of three-dimensional instability, known as the mode B instability, which becomes increasingly disordered as Re is further raised. It was shown in our previous works (Richter, Iaccarino & Shaqfeh 2010; Richter, Shaqfeh & Iaccarino 2011) that viscoelasticity has a profound impact on these mode A and mode B instabilities, which both can be completely suppressed depending on the rheological parameters chosen. This ability to stabilize the early stages of transition in the cylinder wake through the presence of polymeric additives is important from the perspective of both fundamental fluid mechanics as well as engineering applications, and gives rise to a natural extension: How does viscoelasticity affect the later transition stages which occur at higher Reynolds numbers? Characterizing this effect will assist in the further development of polymer injection as a viable flow-altering device in the context of a bluff body

† Email address for correspondence: esgs@stanford.edu

wake. For example, injection of dilute polymer solutions from a marine propeller has been investigated on numerous occasions due to its ability to alleviate the issue of tip vortex cavitation (Chahine, Frederick & Bateman 1993; Fruman, Pichon & Cerrutti 1995; Yakushiji 2009). Therefore, to answer this fundamental question, a study was performed for non-Newtonian flow past a cylinder at $Re = 3900$.

At this Reynolds number, numerous experimental and numerical studies exist for Newtonian flows which largely focus on the instability which develops in the separated shear layers at $Re = O(1000)$. Roshko (1954) was among the first to discover the existence of this unstable shear layer, and later Bloor (1964) made the first measurements of the characteristic frequency of this instability, noting that it was higher than the primary vortex-shedding frequency and that it scaled with Reynolds number. More recently, numerical studies have provided invaluable insight into the cylinder wake at $Re = 3900$: Beaudan & Moin (1994) performed the first large eddy simulation (LES) for this flow; Kravchenko & Moin (2000) also performed LES simulations but using higher-order B-splines, and found improved agreement with the experimental data of Ong & Wallace (1996); Ma, Karamanos & Karniadakis (2000) performed combined LES/DNS (direct numerical simulation) to obtain more accurate turbulence statistics and attempted to resolve the question of the shape of the near-wake mean velocity profile; Parnaudeau *et al.* (2008) performed a combined experimental and numerical study to further improve LES validation; and Rai (2010) studied intermittency of turbulence within the shear layer, motivated by the experimental findings of Prasad & Williamson (1997).

For viscoelastic flows, however, the literature is not nearly as complete. For high Reynolds number flows, nearly all numerical investigations are limited in their focus to some aspect of turbulent drag reduction (see for example Sureshkumar, Beris & Handler 1997; Dimitropoulos, Sureshkumar & Beris 1998; Dimitropoulos *et al.* 2001; Stone *et al.* 2004; Dimitropoulos *et al.* 2006; Kim *et al.* 2007). Ma, Symeonidis & Karniadakis (2003) used their unstructured spectral element formulation to simulate flow over a three-dimensional ellipsoid at $Re = O(1000)$, but their study was limited to low Weissenberg number and emphasized their novel numerical technique rather than physical effects within the wake.

Relevant experimental investigations, similarly, are few in number. Kato & Mizuno (1983) measured drag forces and pressure distributions along the cylinder surface of a flow of dilute polyethylene oxide (PEO) (with molecular weights ranging between 2×10^6 and 4×10^6 g mol^{-1}) at Reynolds numbers up to $Re = 10^5$. In general, reduced drag was seen at high Re with the addition of the polymer solutions, due to a rise in back pressure along the downstream side of the cylinder. Sarpkaya, Rainey & Kell (1973) also performed drag measurements in flows of polyethylene oxide (WSR301) at high Reynolds numbers, but much of the focus of their work was on the effect of additives near the cylinder drag crisis (which occurs in Newtonian flows at $Re = O(10^5)$). Despite this, measurements were still made between $Re = 10^4$ and $Re = 10^5$, and they reported a significant reduction in drag, accompanied by a forward movement of the separation point on the cylinder and a narrowing of the wake (in terms of the y location at which significant velocity fluctuations could be measured) with additions of dilute polymer solutions. Near the drag crisis, they report that polymer additives actually precipitate the onset of this instability, destabilizing the flow within the cylinder boundary layer. Coelho & Pinho (2003*a*,*b*, 2004) performed experiments using two different significantly shear-thinning fluids (methyl hydroxyethyl cellulose (tylose) and carboxymethyl cellulose sodium salt (CMC)), and observed different responses of the flow due to shear thinning versus

elasticity. Reductions in the critical Reynolds numbers which mark the onset of three-dimensional transition as well as shear layer transition were observed, due mainly to the shear-thinning behaviour of the fluid. Contrary to this, they observed that elasticity can suppress the shear layer transition regime and lengthen the recirculation region behind the cylinder. Furthermore, they also measured pressure distributions along the cylinder surface and found that below a Reynolds number of approximately 800, drag was reduced for both fluids, while above 800, the drag was increased. They attributed the drag reduction to a rise in the back pressure, while the drag increase at high *Re* resulted from an eventual transition of the shear layer.

In addition to these, studies have also been performed for high *Re* flow of surfactant solutions past cylinders. Bergins, Nowak & Urban (2001) investigated the wake through Schlieren visualization and laser Doppler velocimetry. They found that for a single solution of tetradecyl trimethyl ammonium salicylate with sodium bromide, the wake structure becomes completely stabilized at a certain critical Reynolds number as *Re* is increased from 270 to 2000. This critical *Re* is associated with the 'shear-induced structure' found in surfactant solutions when micelles form coherent structures in flows with high shear rates. Vortex shedding behind the cylinder is completely suppressed, and the influence of the cylinder is observed far upstream. Similarly, Ogata, Osano & Watanabe (2006) performed measurements of cylinder drag at high Reynolds numbers in flows of oleyl-bihydroxyethyl methyl ammonium chloride at various concentrations and found both drag increases as well as reductions depending on *Re*. At $Re < 2000$, the drag is increased relative to the Newtonian case, due to the large stagnation zone which appears upstream of the cylinder. At higher *Re*, this zone is suppressed and the base pressure rises, reducing the drag.

For the present case, we expect that at Reynolds numbers within the shear layer transition regime, highly elastic (low shear-thinning), dilute polymer solutions will stabilize the flow and inhibit the formation of the turbulent cylinder wake. At Reynolds numbers below the shear layer transition, Cadot & Kumar (2000) observed the suppression of the mode A instability through injection of polyethylene oxide (PEO), which was consistent with the findings of our previous numerical studies (Richter *et al.* 2010, 2011). For higher Reynolds numbers, we can look to studies on the viscoelastic free shear layer to predict the effect within the cylinder wake. For instance, the works of Azaiez & Homsy (1994*a*), Kumar & Homsy (1999) and Yu & Phan-Thien (2004) all indicate that viscoelasticity reduces the Kelvin–Helmholtz rollup instability within a mixing layer, which in the context of the wake would indicate a significant stabilization at sufficiently high Reynolds numbers.

2. Problem formulation

2.1. *Governing equations*

The dimensionless mass and momentum conservation equations in the presence of an extra polymeric stress are presented below:

$$\frac{\partial u_j}{\partial x_j} = 0, \tag{2.1}$$

$$\frac{\partial u_i}{\partial t} + u_j \frac{\partial u_i}{\partial x_j} = -\frac{\partial p}{\partial x_i} + \frac{\beta}{Re}\frac{\partial^2 u_i}{\partial x_j \partial x_j} + \frac{1-\beta}{Re}\frac{1}{Wi}\frac{\partial \tau_{ij}^p}{\partial x_j}. \tag{2.2}$$

The flow Reynolds number, $Re = \rho U_\infty D/(\mu_p + \mu_s)$, is based on the cylinder diameter D, the free-stream velocity U_∞, the fluid density ρ, and the total solution zero-shear-rate viscosity μ_T, made up from a polymer contribution μ_p and a solvent contribution

μ_s. Similarly the Weissenberg number, $Wi = \lambda U_\infty / D$, is based on the diameter D and free-stream velocity U_∞, as well as the polymer relaxation time λ, and represents the ratio of the polymeric stress relaxation time scale to the convective time scale of the flow. Finally, the parameter $\beta = \mu_s/(\mu_p + \mu_s)$ represents the contribution of the solvent viscosity to the total solution viscosity.

As was done in previous studies of the viscoelastic cylinder wake (Richter *et al.* 2010, 2011), closure of the momentum equation was achieved by employing the FENE-P model to represent the extra stress τ_{ij}^p:

$$\tau_{ij}^p = \frac{c_{ij}}{1 - \dfrac{c_{kk}}{L^2}} - \delta_{ij}. \tag{2.3}$$

The FENE-P model introduces a maximum length which bounds polymer stresses, and this is manifested in the above equation through the polymer extensibility L. Furthermore, c_{ij} is the polymer conformation tensor, and is subject to an evolution equation derived from a balance of stretching and spring restoring forces within the bead-spring approximation of a single polymer:

$$\frac{\partial c_{ij}}{\partial t} + u_k \frac{\partial c_{ij}}{\partial x_k} - c_{ik}\frac{\partial u_j}{\partial x_k} - c_{kj}\frac{\partial u_i}{\partial x_k} = -\frac{1}{Wi}\tau_{ij}^p. \tag{2.4}$$

This viscoelastic representation assumes a dilute, homogeneous polymer concentration throughout the flow field, and has been proved to elucidate essential physical processes in other high Reynolds number, non-Newtonian flows (see for example Sureshkumar *et al.* 1997; Kumar & Homsy 1999; Dimitropoulos *et al.* 2006).

2.2. *Numerical method*

To solve the ten governing equations presented in the previous section, the same code described in Richter *et al.* (2010) was utilized. Only a brief description of the method will be given here; further details can be found in previous works (Richter *et al.* 2010, 2011).

The code is based on an unstructured, finite-volume formulation using a fractional step approach to satisfy the incompressibility (divergence-free velocity) condition. Velocity and scalar derivatives are discretized with central differencing, with the exception of scalar convective derivatives (i.e. derivatives of the c_{ij} components within the advection term), which are discretized using quadratic upwinding (QUICK). The solution is advanced in time with the second-order Crank–Nicolson scheme. The time step is chosen with a constant dimensionless Δt, set at $\Delta t = 0.0045$ for Newtonian simulations and $\Delta t = 0.002$ for viscoelastic simulations (note that when comparing this to the fluid relaxation time, λ is equal to Wi since both the diameter D and upstream velocity U_∞ are set to 1.0)

As described in Richter *et al.* (2010), the method introduced by Dubief *et al.* (2005) to limit polymer stretch to the maximum extensibility L is used to guarantee polymer stretch and stress boundedness at each time step, resulting in a robust numerical scheme which can simulate high Reynolds number, high Weissenberg number, and high polymer extensibility flows. It should be noted that for numerical stability, global artificial diffusion is introduced for the components of c_{ij}, and the resulting Schmidt number ($Sc = \nu_T/\Gamma$, the ratio of total solution kinematic viscosity to scalar diffusion) is equal to 0.77 throughout this study. In previous studies of unsteady viscoelastic flows, the effect of artificial diffusion for c_{ij} has been investigated, and was seen to have little effect when $Sc = O(1)$ (Dubief *et al.* 2005; Richter *et al.* 2010).

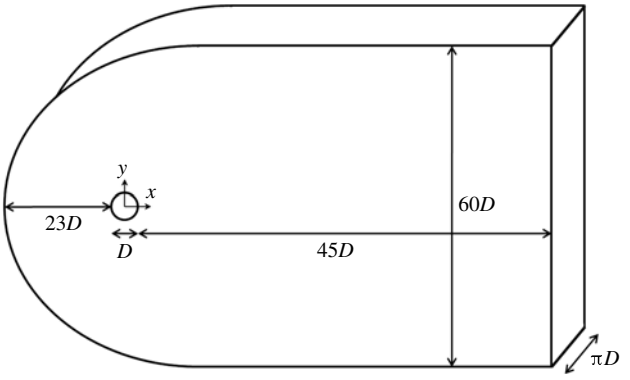

FIGURE 1. Schematic of the computational domain.

Furthermore, Yu & Phan-Thien (2004) looked specifically at the effect of artificial diffusion for the FENE-P model in a high Reynolds number, viscoelastic mixing layer, and found that although a small amount of smoothing of polymer stress gradients was observed, it did not have an overall negative effect on the dynamics studied. They tested multiple schemes for introducing their diffusion (both a constant and adaptive diffusivity), and for the coarsest mesh used their Schmidt number, as defined above, is approximately $Sc \approx 6$. For the current case, we anticipate that for higher Schmidt numbers, gradients of c_{ij} would merely grow stronger locally, while the underlying mechanisms found in this study will still be active (and perhaps even stronger due to sharper polymer stress gradients).

2.3. *Geometry and boundary conditions*

A schematic of the domain used to study the flow over an unbound cylinder is shown in figure 1. The domain extends $23D$ radially upstream and $45D$ downstream of the cylinder in the xy plane. No-slip conditions for the velocity ($u_i = 0$) and no-flux conditions for the conformation tensor ($\partial c_{ij}/\partial n = 0$) are specified along the cylinder surface. Along the curved inlet upstream of the cylinder as well as along the horizontal surfaces above and below the wake, the free-stream velocity is set to be $U_\infty = [1, 0, 0]$, and the conformation tensor is set to the near-equilibrium value of $c_{ij} = \delta_{ij}$ (stress-free equilibrium implies $c_{ij} = \delta_{ij}$ only as $L \to \infty$, but only small differences exist for $L = O(10)$ and above). Along the vertical outlet plane, convective outlet conditions are used for both u_i and c_{ij}. The spanwise extent is πD, and periodic boundary conditions are applied to all flow quantities in the z direction.

3. Validation

At a Reynolds number of 3900, turbulence dominates the flow field, and therefore a wide range of spatial and temporal scales exist throughout the cylinder wake. Typical Newtonian studies in this Reynolds number regime consist of large eddy simulations (LES), using a subgrid model to account for unresolved dissipative motions beyond those that the computational mesh can explicitly represent (see for instance Beaudan & Moin 1994; Kravchenko & Moin 2000; Parnaudeau *et al.* 2008). For the present study, however, the flow is computed without any sub-grid model, since its formulation in the presence of an active scalar (viscoelasticity) is uncertain at best. In fact, in their work, Kravchenko & Moin (2000) compared simulations with and without subgrid models,

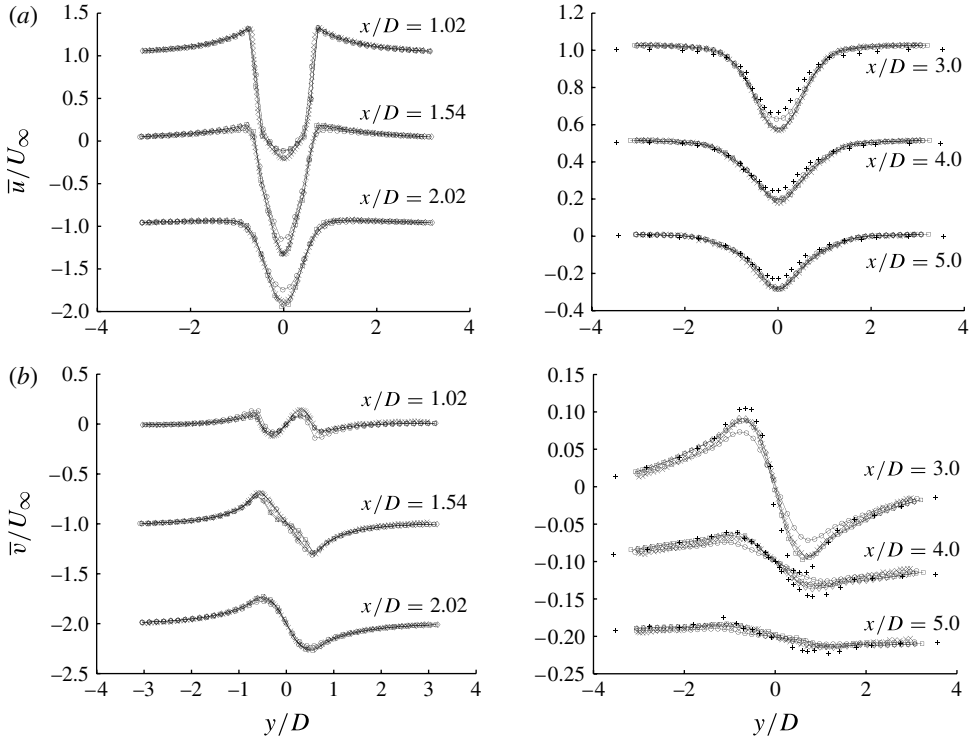

FIGURE 2. Mean (a) streamwise and (b) transverse velocity profiles in the near and far wake. Data are shown for three spanwise grid resolutions, as well as that from Kravchenko (1998). Far-wake profiles are also compared to experimental data of Ong & Wallace (1996). Symbols are as follows: ×, Kravchenko (1998); +, Ong & Wallace (1996); ∘, $N64$; □, $N80$; ◇, $N128$. Overbar indicates average over the span and time (at least 20 shedding cycles). (a) $\overline{u}/U_\infty$; (b) $\overline{v}/U_\infty$.

and reported small influences of the presence of the model. Furthermore, Rai (2008) performed simulations on grids comparable in size to those used for LES, but using no subgrid model, and his results suggest that turbulence statistics and spectra could be well reproduced for high-order upwinding schemes. Therefore, to ensure that the absence of a subgrid model does not negatively impact the results for the present study, validation of the numerical formulation will be illustrated based on mesh-converged mean flow profiles and spectra for a Newtonian fluid, as well as their comparison with existing experimental and numerical data.

Overall, the computational mesh is unstructured, and has a minimum spacing at the cylinder surface of $\Delta r = 0.0015D$ and $\Delta\theta = 0.027$ radians. In the xy plane, the mesh is the same as that used in Richter *et al.* (2010). Mesh convergence was done through a refinement of the spanwise grid spacing. As mentioned above, the spanwise domain size is πD, and the notation in the following figures is as follows: $N64$ refers to 64 spanwise grid points, $N80$ to 80 grid points, etc. Figure 2 shows mean streamwise and transverse velocity profiles and figure 3 shows streamwise and transverse velocity fluctuation profiles at several downstream locations for three different mesh sizes, as well as the experimental results of Ong & Wallace (1996) and LES results of Kravchenko (1998). It is clear that for these quantities, all three mesh resolutions generally do well representing the mean flow characteristics both in the near- and

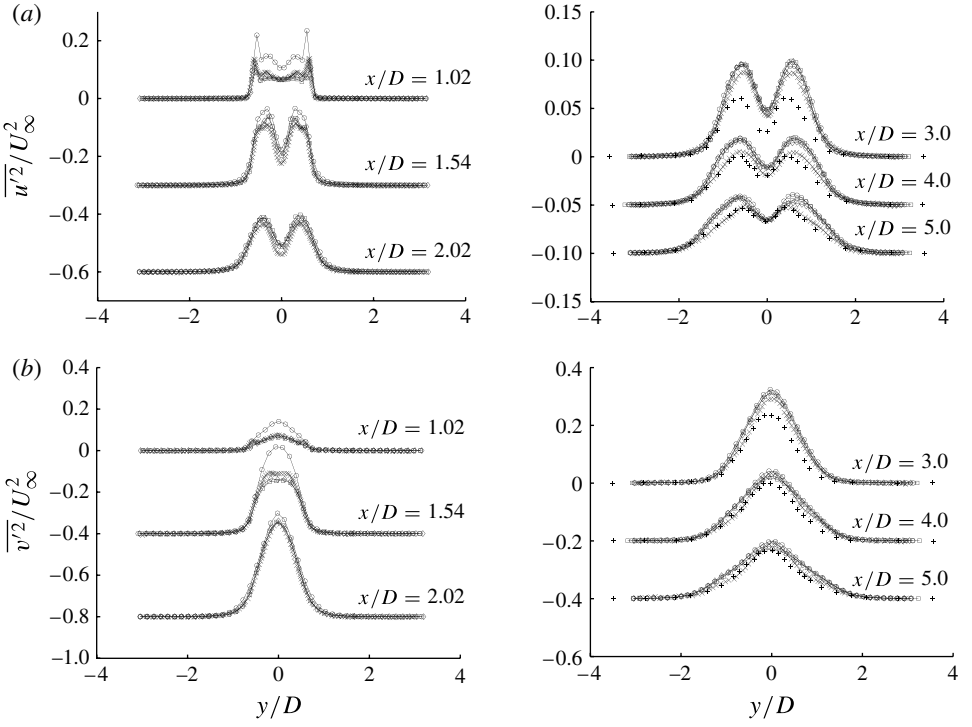

FIGURE 3. Mean (*a*) streamwise and (*b*) transverse velocity fluctuation profiles in the near and far wake. Data are shown for three spanwise grid resolutions, as well as that from Kravchenko (1998). Far-wake profiles are also compared to experimental data of Ong & Wallace (1996). Symbols are as follows: ×, Kravchenko (1998); +, Ong & Wallace (1996); ∘, *N*64; □, *N*80; ⋄, *N*128. Overbar indicates average over the span and time (at least 20 shedding cycles). (*a*) $\overline{u'^2}/U_\infty^2$; (*b*) $\overline{v'^2}/U_\infty^2$.

far-wake regions. The largest discrepancies that exist between the *N*64 mesh and the *N*80 and *N*128 meshes are located near the edge recirculation bubble, and this is a direct result of a difference of within 5 % in the bubble's computed length. This result is not surprising based on the findings of Kravchenko & Moin (2000). Downstream of the bubble region, seen in profiles taken at $x/D > 3.0$, all mesh resolutions perform very well compared to both experiments and previous numerical LES calculations.

In addition to using mean flow profiles to assess the accuracy of the flow field, streamwise and transverse one-dimensional energy spectra taken at several downstream locations were also computed to compare with the works of Ong & Wallace (1996) and Kravchenko (1998). This is shown in figure 4. In the figure, the spanwise-averaged energy spectra $\overline{E}_{11}$ and $\overline{E}_{22}$ are non-dimensionalized by $U_\infty^2 D$ and are plotted against frequency, which is non-dimensionalized by the primary vortex-shedding frequency (f_{St}). The dominant peak in the $\overline{E}_{11}$ spectrum indicates the primary vortex-shedding frequency, and lies at $f/f_{St} = 2.0$ since streamwise energy fluctuations repeat every half shedding cycle. The dominant peak in the $\overline{E}_{22}$ spectrum also indicates the primary shedding frequency (now at $f/f_{St} = 1.0$, since transverse fluctuations repeat every full cycle), and this peak is followed by a second, harmonic peak located at $f/f_{St} = 3.0$.

Figure 4 shows that as the spanwise grid spacing is refined, very little improvement is gained in the spectra. Furthermore, spectra taken farther from the cylinder become

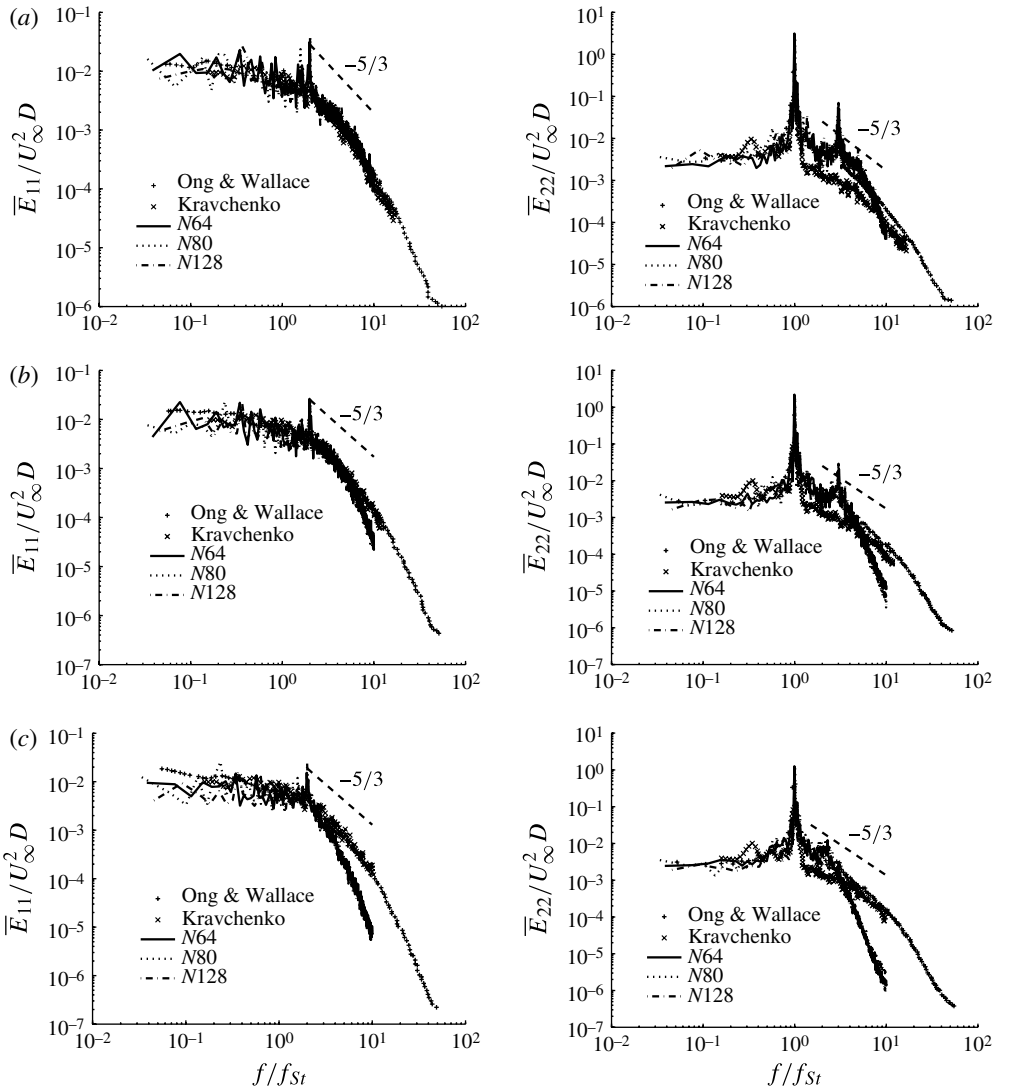

FIGURE 4. Newtonian dimensionless energy spectra $\overline{E}_{11}/U_\infty^2 D$ and $\overline{E}_{22}/U_\infty^2 D$ at several downstream locations for three different spanwise grid resolutions. Computed data compared to the experimental measurements of Ong & Wallace (1996) and the LES of Kravchenko (1998). Frequency normalized with Strouhal frequency. Overlines in the case of energy spectra $\overline{E}_{11}$ and $\overline{E}_{22}$ indicate spanwise averaging. (*a*) $x/D = 5.0$; (*b*) $x/D = 7.0$; (*c*) $x/D = 10.0$.

more and more numerically dissipative at small scales, illustrated by the premature drop-off in the computed spectra relative to the data of Ong & Wallace (1996) and Kravchenko (1998). Near the cylinder (especially $x/D = 5$), excellent quantitative agreement is found over the entire frequency range, while by $x/D = 7$, and even more so for $x/D = 10$, the grid in the xy plane becomes too coarse to resolve all energy content at any spanwise grid spacing. For reference, Beaudan & Moin (1994) quote values of the Kolmogorov length scale (η_K) at 3 downstream locations along the wake centreline. These values are included in table 1, along with the corresponding

	η_K/D	$\Delta x/\eta_K$	$\Delta y/\eta_K$	$\Delta z/\eta_K$
Shear layer	8.81×10^{-3}	2.8	1.3	4.4
$x/D = 3.0$	8.81×10^{-3}	7.9	1.6	4.4
$x/D = 5.0$	8.81×10^{-3}	13.6	1.6	4.4
$x/D = 7.0$	9.11×10^{-3}	17.5	1.5	4.3
$x/D = 10.0$	10.1×10^{-3}	22.7	1.3	3.9

TABLE 1. Values of the Kolmogorov length η_K/D from Beaudan & Moin (1994) and the corresponding ratios of η_K to grid spacing at different locations within the wake.

values of $\Delta x/\eta_K$, $\Delta y/\eta_K$, and $\Delta z/\eta_K$ at the same locations. Values are also included at $x/D = 3.0$ and within the shear layer, assuming that η_K/D is the same as that at $x/D = 5.0$. Furthermore, one can also compute the Kolmogorov time scale τ_K, which at its minimum is $\tau_K \approx 0.3$, which is well above the time step used in all simulations. It is also worth mentioning for the sake of comparison that the spectral element simulations of cylinder flow at $Re = 3900$ by Ma *et al.* (2000), which they cite as being fully resolved DNS, use for their finest grid resolution 902 spectral elements in the xy plane (of polynomial order 10, resulting in a number of degrees of freedom up to 1×10^8) and 128 Fourier modes in the z direction.

For the purpose of this study, which is to investigate the effect of viscoelasticity on the near-wake, these comparisons to experimental and LES data are considered fully acceptable, since mechanisms of viscoelastic stability are ultimately found in the near-wake region and are not dominant in regions which are not fully mesh-resolved. Moreover, it has been observed in past turbulent, viscoelastic channel flow simulations that the presence of viscoelasticity attenuates the energy spectra, requiring less resolution at a given Reynolds number than its Newtonian counterpart (see Dubief *et al.* 2005), thus alleviating any deficiency in the current mesh at representing all spatial and temporal scales. As will be illustrated later, this is indeed the case. Therefore, for nearly all simulations presented, 80 grid points over a spanwise length of πD were used in the z direction. Due to the large computational times required, the exceptions to this are the two simulations done at Weissenberg numbers other than 10 (those presented later in figures 11 and 12), which use 64 points in the z direction.

4. Numerical results

Before presenting the effects which viscoelasticity has on the detached shear layer and wake of the cylinder, it is instructive to first examine various flow parameters. Table 2 shows how the vortex-shedding frequency (non-dimensionalized by U_∞/D to create a Strouhal number), average drag coefficient, $\overline{C}_D$, and its components (viscous, pressure, and viscoelastic) change with increasing values of polymer extensibility L. Also contained in this table are the values of $\overline{C}_D$ and St obtained by Kravchenko & Moin (2000) for Newtonian flow at the same Re for comparison.

As the polymer extensibility L is increased, there is a slight (2 %) reduction in $\overline{C}_D$ at $L = 10$, followed by a 12 % increase as L approaches 100. This non-monotonic response of the drag versus increasing L is similar to the behaviour found at a much lower Reynolds number ($Re = 100$; see Richter *et al.* 2010), and its causes are similar as well. Figure 5 shows average values of pressure coefficient $\overline{C}_p = 2(\overline{p} - p_\infty)/\rho U_\infty^2$, viscoelastic local shear stress, and viscoelastic local normal stress over the cylinder surface. From figure 5(*a*) it is immediately clear that as the polymer extensibility is

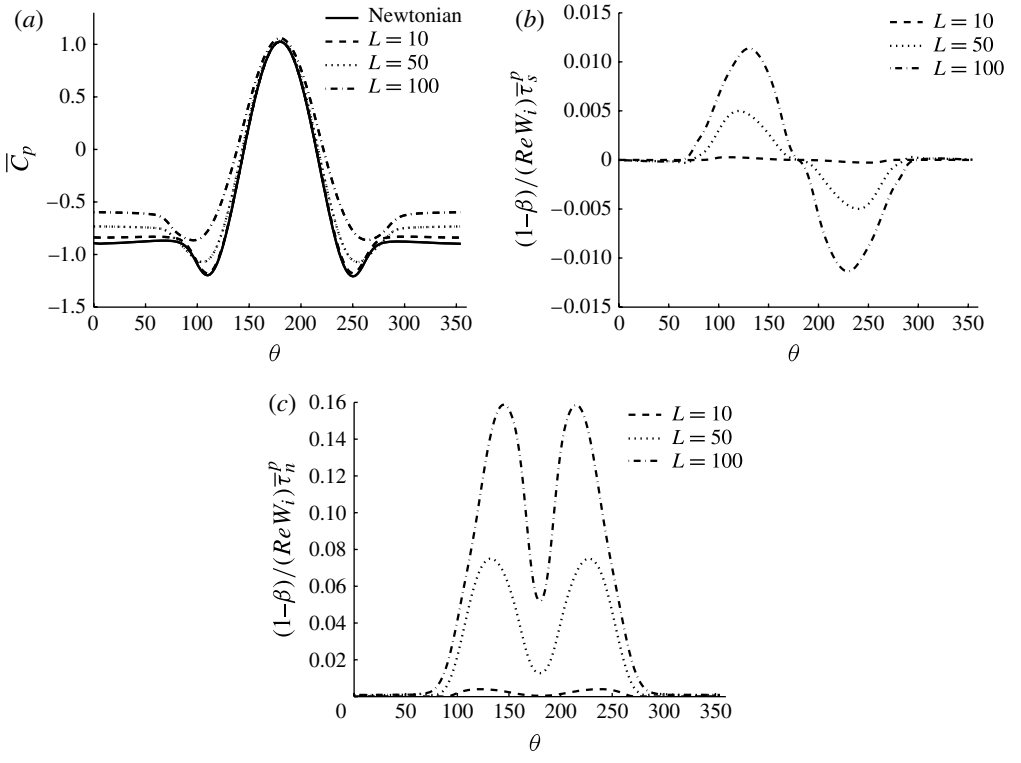

FIGURE 5. Stress components versus angle θ (in degrees) along cylinder surface. (*a*) Average pressure coefficient $\overline{C}_p = 2(\overline{p} - p_\infty)/\rho U_\infty^2$. (*b*) Average local shear component of viscoelastic stress $\overline{\tau}_s^p$, multiplied by $(1-\beta)/(ReWi)$. (*c*) Average local normal component of viscoelastic stress $\overline{\tau}_n^p$, multiplied by $(1-\beta)/(ReWi)$. θ is measured anticlockwise from the rear stagnation point.

	$\overline{C}_D$	$\overline{C}_D^{viscous}$	$\overline{C}_D^{pressure}$	$\overline{C}_D^{polymer}$	St
Newtonian	0.984	0.044	0.940	—	0.211
$L = 10$	0.965	0.041	0.921	0.004	0.216
$L = 50$	0.990	0.027	0.895	0.068	0.218
$L = 100$	1.103	0.011	0.917	0.174	0.189
Kravchenko & Moin (2000)	1.04	—	—	—	0.210

TABLE 2. Average drag coefficient $\overline{C}_D$ and its components $\overline{C}_D^{viscous}$, $\overline{C}_D^{pressure}$, and $\overline{C}_D^{polymer}$, as well as dimensionless vortex-shedding frequency for increasing polymer extensibility L. The values of $\overline{C}_D$ and St from Kravchenko & Moin (2000) are included as well.

increased, the pressure on the downstream side of the cylinder increases monotonically, which, by itself, would lower the drag as in the case for $L = 10$. As L is increased, however, two factors offset this rear pressure rise: an additional viscoelastic drag ($\overline{C}_D^{polymer}$, representing polymer stresses acting directly on the cylinder surface) and a rise in the forward stagnation pressure. This effect is most obvious for $L = 100$, where the pressure component is larger than that of the Newtonian case, and the viscoelastic

component becomes a significant fraction (nearly 20 %) of the total drag. As seen in figures 5(*b*) and 5(*c*), the surface values of viscoelastic stress (both shear and normal components) are centralized on the upstream side of the cylinder, between the forward stagnation point and the cylinder top/bottom. With an increase of L, these stresses are amplified while maintaining a similar shape, and for $L = 100$ approach an order of magnitude similar to that of the pressure stress. Finally, the increase of the form drag as polymer extensibility is increased was discussed in detail in Richter *et al.* (2010), and results from a region of large, 'solid-like' polymer stress at the forward stagnation point.

Of the few experiments that exist for polymeric flows past a cylinder at high Reynolds number, Kato & Mizuno (1983) measured average values of drag as well as pressure distributions over the cylinder surface over a very wide range of Re, and in general found reductions in $\overline{C}_D$ over the range $10^3 < Re < 10^5$. Focusing on $Re \approx 3900$, they show that for three different molecular weights of PEO (2×10^6, 3×10^6, and 4×10^6 g mol^{-1}), the reduction in drag is non-monotonic for increasing polymer concentration. Furthermore, they see that the reductions in drag are due to a rise in the back pressure, agreeing with the present simulations, and that for high concentrations there is a slight increase in the forward stagnation pressure. While they do not ultimately see an increase in drag as in the present results for large L, their non-monotonic behaviour of the drag with increasing concentration appears to be consistent with our results: as the solutions become more elastic at high concentrations, the back pressure rise and corresponding drag reduction begins to be offset by an increased forward stagnation pressure. Moreover, they assume the form drag is the only component of the total drag. Based on table 2, this assumption is justified in neglecting the Newtonian viscous stresses on the cylinder, but the polymer stresses acting on the surface may be significant.

In addition to this, Coelho & Pinho (2004) measured increasing drag with increasing Re, falling below that of Newtonian flow for Re less than approximately 1000 and above for Re larger than 1000. This modest increase in drag would agree with the high L case seen in the current study, but even qualitative comparisons are difficult due to the high degree of shear thinning in the fluids used in their study (a fluid property not strongly present in our numerical model). Ogata *et al.* (2006) also see back pressure increases competing with upstream elastic effects, but this is for phenomena associated with micelle solutions and caution should be taken when relating these effects to the current numerical results.

4.1. *Wake stabilization*

When adding the effects of viscoelasticity, profound changes are identified in the wake as the polymer extensibility is increased. Figure 6 illustrates this qualitatively, showing surfaces of constant streamwise vorticity at $\omega_x = \pm 3.0$. For the Newtonian case (figure 6*a*), the entire wake has transitioned to turbulence, due to the turbulent shear layer immediately behind the cylinder. For a short polymer extensibility of $L = 10$ (figure 6*b*), no significant changes are seen in the structure of the wake. This is similar to the findings of Richter *et al.* (2010, 2011); additional polymeric stresses at $L = 10$ do not have sufficient magnitude to exert significant changes in the turbulent flow structures. As the polymer extensibility is increased further, however, a dramatic change in the morphology of the wake emerges. At $L = 50$ and more so at $L = 100$, the wake suddenly becomes much more coherent in nature, displaying not only an extended recirculation region (also seen in the previous Reynolds number analyses of Richter *et al.* 2010), but a streamwise vorticity structure reminiscent of the mode B

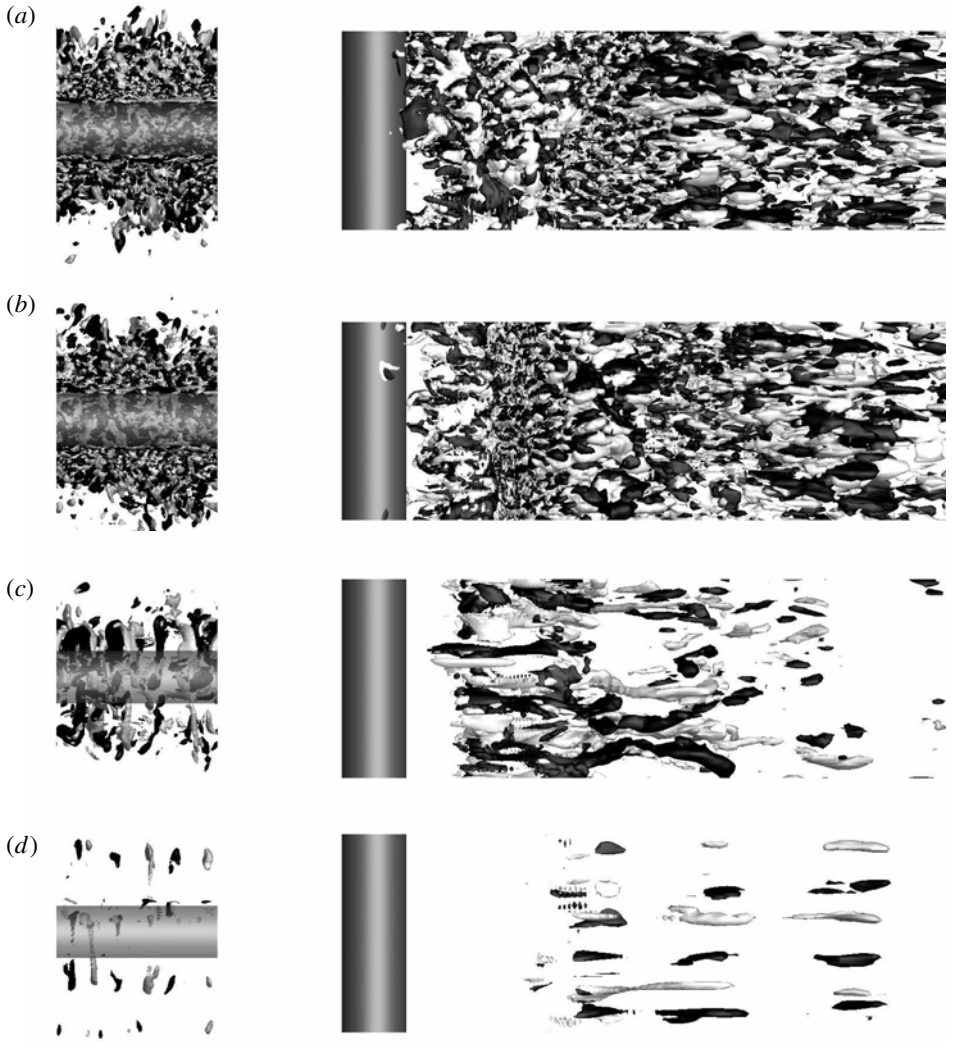

FIGURE 6. Instantaneous streamwise vorticity isosurfaces ($\omega_x = \pm 3.0$) in $Re = 3900$ flow. (*a*) Newtonian; (*b*) $Wi = 10$, $L = 10$, and $\beta = 0.9$; (*c*) $Wi = 10$, $L = 50$, and $\beta = 0.9$; (*d*) $Wi = 10$, $L = 100$, and $\beta = 0.9$. The left image is looking through the cylinder in the downstream direction and the right image is the view from above the wake.

instability seen at much lower Reynolds numbers in Newtonian flows (see Williamson 1996*a* for a description of the mode B instability). The alternating streaks of positive and negative vorticity possess the correct symmetry and roughly the proper wavelength to match that of the mode B hyperbolic instability, and thus it would appear that viscoelasticity has delayed the Newtonian modes of turbulent transition.

To get a more quantitative view of this effect, one-dimensional energy spectra taken at several locations downstream are plotted in figure 7. For the $L = 10$ case, no detectable change in the energy content is found at any point downstream, consistent with the qualitative evidence found in figure 6. For $L = 50$ and $L = 100$, energy content, especially for that of $\overline{E}_{11}$, is diminished by up to two orders of magnitude along the entire wake extent. This again shows that small-scale turbulent energy is

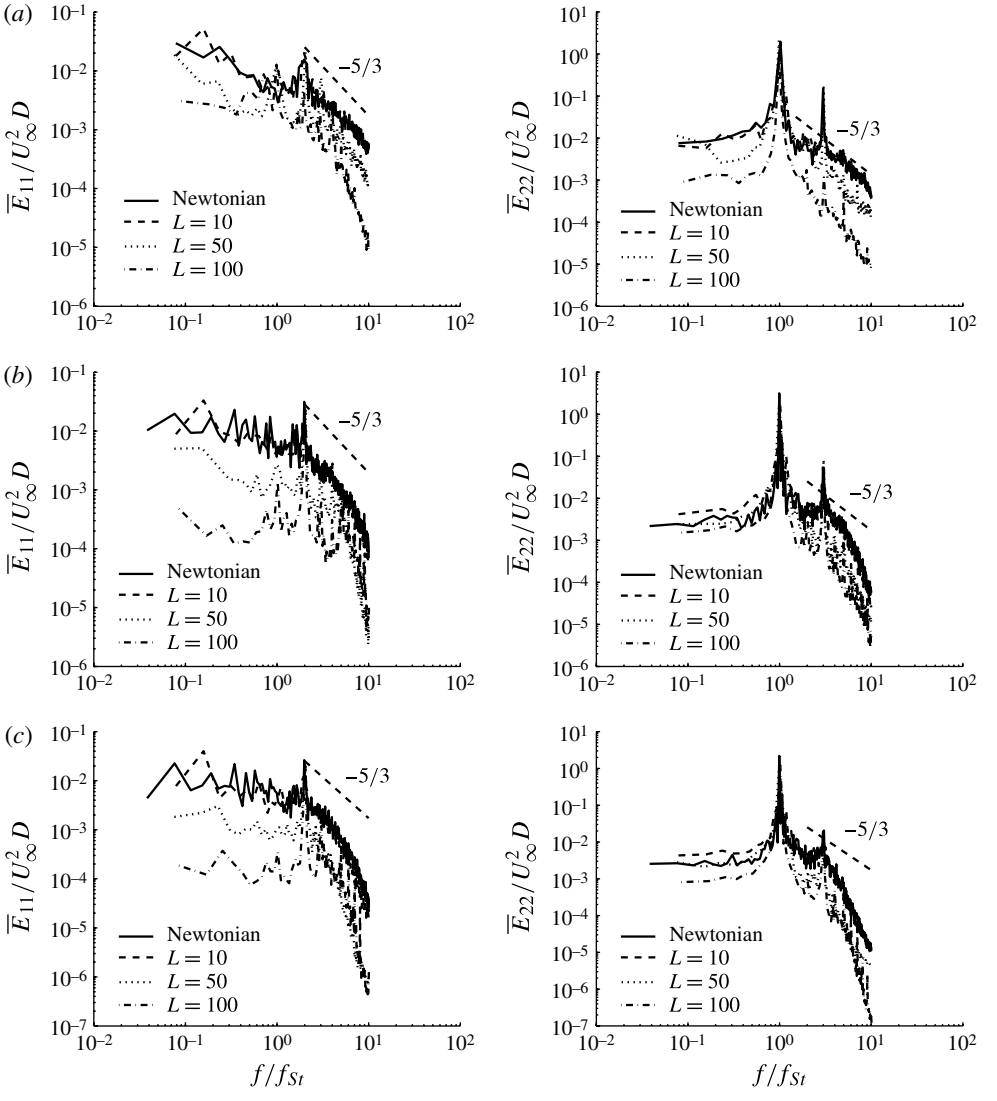

FIGURE 7. Dimensionless energy spectra $\overline{E}_{11}/U_\infty^2 D$ and $\overline{E}_{22}/U_\infty^2 D$ at several downstream locations. Viscoelastic computations are at $Wi = 10$, $\beta = 0.9$, and varying L between $L = 10$, $L = 50$, and $L = 100$. Frequency normalized with Strouhal frequency. Overlines in the case of energy spectra $\overline{E}_{11}$ and $\overline{E}_{22}$ indicate spanwise averaging. (*a*) $x/D = 3.0$; (*b*) $x/D = 5.0$; (*c*) $x/D = 7.0$.

being nearly eliminated in the entire wake, suggesting a dramatic stabilization due to the presence of viscoelasticity.

5. Mechanism

In general, viscoelasticity has previously been seen through numerical studies to have a stabilizing effect on rollup instabilities found in mixing layers (Azaiez & Homsy 1994*a*,*b*; Kumar & Homsy 1999; Yu & Phan-Thien 2004). Depending on the Reynolds number and Weissenberg numbers found locally in the layer, both two-

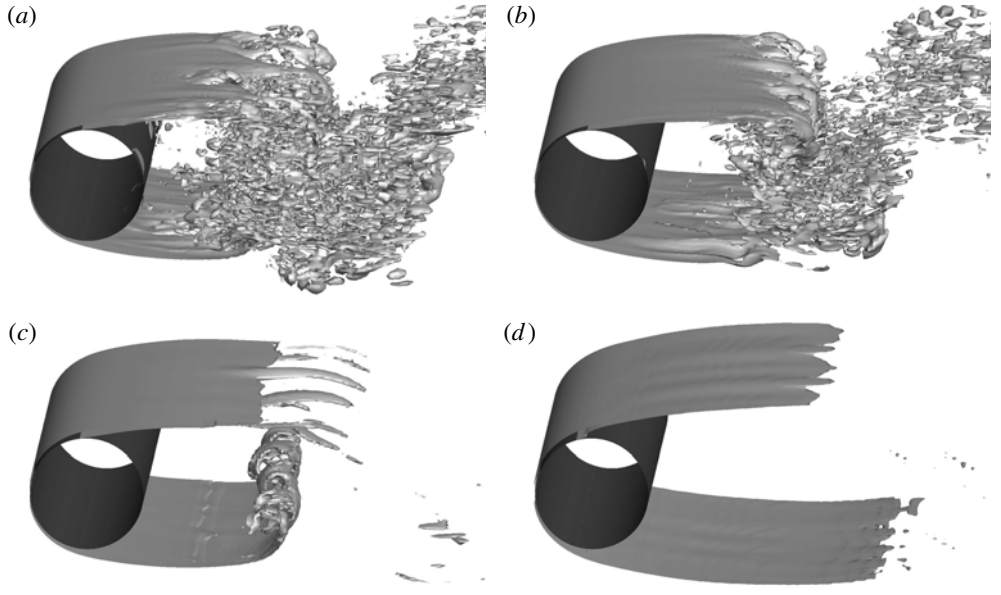

FIGURE 8. Instantaneous spanwise vorticity isosurfaces ($\omega_z = \pm 9.0$) in $Re = 3900$ flow, focused on separated shear layer. (*a*) Newtonian; (*b*) $Wi = 10$, $L = 10$, and $\beta = 0.9$; (*c*) $Wi = 10$, $L = 50$, and $\beta = 0.9$; (*d*) $Wi = 10$, $L = 100$, and $\beta = 0.9$.

dimensional as well as subsequent three-dimensional transition modes are inhibited by the presence of elasticity. Therefore, we will direct our focus to this location when searching for a wake stabilizing mechanism.

Figure 8 shows surfaces of spanwise vorticity at $\omega_z = \pm 7.0$ in the region immediately downstream of the cylinder. With increasing polymer extensibility, the effect of viscoelasticity is clear: the instabilities which form in the shear layer for the Newtonian case are suppressed under the influence of high elasticity, in agreement with predictions from viscoelastic shear layer studies. From this, it can also be concluded that for the $L = 10$ case, changes to the wake structure were not observed in figure 6 due to its inability to fully stabilize the mixing layer, prior to primary vortex shedding. This effect is entirely consistent with two of the few experimental studies devoted to the viscoelastic shear layer. Both Riediger (1989) and Hibberd, Kwade & Scharf (1982) observed, through flow visualization, reduced levels of small-scale turbulence in a mixing layer containing polymer or surfactant additives, as well as stronger and more persistent large-scale structures. More importantly, however, the figures in both studies comparing the viscoelastic to Newtonian shear layers show that the non-Newtonian mixing layer takes noticeably longer to develop these coherent structures (in terms of distance from the splitter plate), which, in the case of the cylinder wake, indicates that stabilization of the shear layer could certainly be achieved before the primary vortex is shed.

Bloor (1964) was the first to measure the characteristic instability frequency found in a transitioning shear layer behind a cylinder, noting that it was greater than that of the primary vortex-shedding frequency. For energy spectra taken within this layer, its presence is therefore manifested as a broad peak located at higher frequencies than the primary vortex peak. This is illustrated very clearly by Prasad & Williamson (1997), and as a result, $\overline{E}_{11}$ and $\overline{E}_{22}$ spectra were taken at similar locations in the present

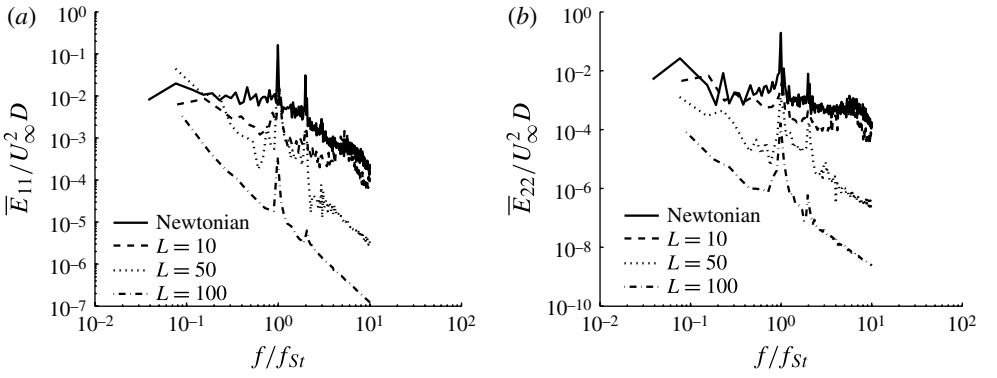

FIGURE 9. Dimensionless energy spectra $\overline{E}_{11}/U_\infty^2$ and $\overline{E}_{22}/U_\infty^2$ taken within the shear layer immediately behind the cylinder, comparing Newtonian energy spectra to viscoelastic computations with $Wi = 10$, $\beta = 0.9$, and varying L between $L = 10$, $L = 50$, and $L = 100$. Frequency normalized with Strouhal frequency. Note the pronounced shear layer frequency peak around $f/f_{St} \approx 6$ for Newtonian and $L = 10$ flow.

study to observe the evolution of this peak with increasing elasticity. Figure 9 contains these plots, and for Newtonian flow, this broad shear layer instability peak is plainly visible at $f_{SL}/f_{St} \approx 6.0$, where f_{SL} is the shear layer instability frequency and recalling that f_{St} is the primary Strouhal (primary vortex) frequency. For $L = 10$, it is interesting to note a diminished magnitude of energy content throughout the range of scales, but both spectra still exhibit a pronounced instability occurring in the shear layer. This indicates that the shear layer still transitions, just not as energetically. For $L = 50$ and $L = 100$, it is not surprising to see this instability peak eliminated, illustrating that viscoelasticity is truly affecting the wake dynamics, beginning as early as within the detached shear layers.

To relate the stabilization seen in the $Re = 3900$ cylinder wake to the studies of Azaiez & Homsy (1994*a*,*b*), Kumar & Homsy (1999) and Yu & Phan-Thien (2004), local values of the Reynolds and Weissenberg numbers were computed using quantities from the separated shear layers:

$$Re_\delta = \frac{2U_0\delta}{\nu_T}, \tag{5.1}$$

$$Wi_\delta = \frac{\lambda\nu_T}{\delta}. \tag{5.2}$$

In these local definitions, δ is a measure of the shear layer thickness, and U_0 is one-half the velocity difference across the shear layer. These lead to a quantity known as the elasticity number, which is the ratio of the Weissenberg number to Reynolds number:

$$E_\delta = \frac{Wi_\delta}{Re_\delta} = \frac{\lambda\nu_T}{\delta^2}. \tag{5.3}$$

Note that for all cases shown thus far, the Weissenberg number based on the cylinder diameter has been set to $Wi = 10$, leading to a relaxation time of $\lambda = 10$ since $D = 1$ and $U_\infty = 1$. As a result, the differences in the values of Re_δ and Wi_δ between cases as L is increased are entirely due to the changes in the mixing layer thickness δ, which for the cases presented below is calculated as the difference in the locations above and

below the shear layer where the spanwise vorticity ω_z is 10 % of maximum vorticity in the layer. For Newtonian, $L = 10$, and $L = 50$ flow, $Re_\delta \approx 570$, while for the $L = 100$ case, it was reduced to $Re_\delta \approx 370$. Similarly, Wi_δ for the $L = 10$ and $L = 50$ cases was close: $Wi_\delta \approx 110$, leading to an elasticity number of $E_\delta \approx 0.2$. For the $L = 100$ case, $Wi_\delta \approx 150$, leading to an elasticity number of $E_\delta \approx 0.4$.

In their linear stability analysis, Azaiez & Homsy (1994*a*) found that in the inviscid limit while the elasticity number was maintained at $E_\delta = O(1)$, growth rates of the rollup instability were inhibited by the presence of viscoelasticity. This was due to a phase shift in the source and sink regions of vorticity production as viscoelasticity (E_δ) was increased, which ultimately led to the inability of vorticity to form a single core. This mechanism was further confirmed by Kumar & Homsy (1999), who quantified this phase shift as a broadening of the range of frequency content contained along a viscoelastic shear layer versus its Newtonian counterpart. This increased frequency content has in fact been observed experimentally by Sausset, Cadot & Kumar (2004), and prevents the dominant instability mode from growing. Kumar & Homsy (1999) also identified through their full simulation of the rollup process two parameter regimes which could lead to inhibited vortex formation: (i) at high polymer extensibility L and (ii) when the elasticity number is $E_\delta = O(1)$ and higher. These two regimes will be related to the present study one at a time.

We have already demonstrated in figures 8 and 9 that the separated shear layer immediately behind the cylinder can be stabilized, even in the presence of relatively low elasticity numbers, as long as the extensibility L is sufficiently large ($E_\delta = 0.4$ for $L = 100$). High L leads to large normal stress gradients, which was what Kumar & Homsy (1999) identified as being a critical component to rollup inhibition. To quantify this effect, the viscoelastic contribution to the evolution of spanwise vorticity (the viscoelastic term of the ω_z equation) was computed within the separated shear layers:

$$T_z^v = \frac{1-\beta}{Re}\frac{1}{Wi}\left[\frac{\partial}{\partial x}\left(\frac{\partial \tau_{2k}^p}{\partial x_k}\right) - \frac{\partial}{\partial y}\left(\frac{\partial \tau_{1k}^p}{\partial x_k}\right)\right]. \tag{5.4}$$

T_z^v is the spanwise component of the 'polymer torque' discussed by Kim *et al.* (2007), and represents the amount of resistance to rotational motion due to the local presence of viscoelasticity. This viscoelastic source (or sink) is clearly dependent on polymer stress gradients as well as the Weissenberg number. Contours of this polymer torque are shown in figure 10 for the $L = 10$ and $L = 100$ cases. Solid lines show contours of spanwise vorticity ω_z.

From figure 10(*a*) it is observed that low values of L do not produce values of T_z^v large enough to inhibit rollup. At the location of shear layer breakdown, only modest levels of polymer torque are observed, and they clearly do not prevent the instability from forming. For $L = 100$, however (figure 10*b*), a unique pattern of T_z^v forms midway downstream within the shear layer: for the upper shear layer, a region of high positive T_z^v (vorticity source) lies on top of a region of low negative T_z^v (vorticity sink), and this top/bottom combination repeats itself several times in the downstream direction with a characteristic wavelength of the order of the shear layer thickness (note that for the bottom shear layer, a vorticity sink lies above a vorticity source). From the discussions of Azaiez & Homsy (1994*a*) and Kumar & Homsy (1999), we can immediately confirm what is happening in the case of high L. Azaiez & Homsy (1994*a*) found through their linear stability analysis that with increasing viscoelasticity, the regions of vorticity and velocity perturbations which, acting together, are responsible for the rollup instability, become skewed and less

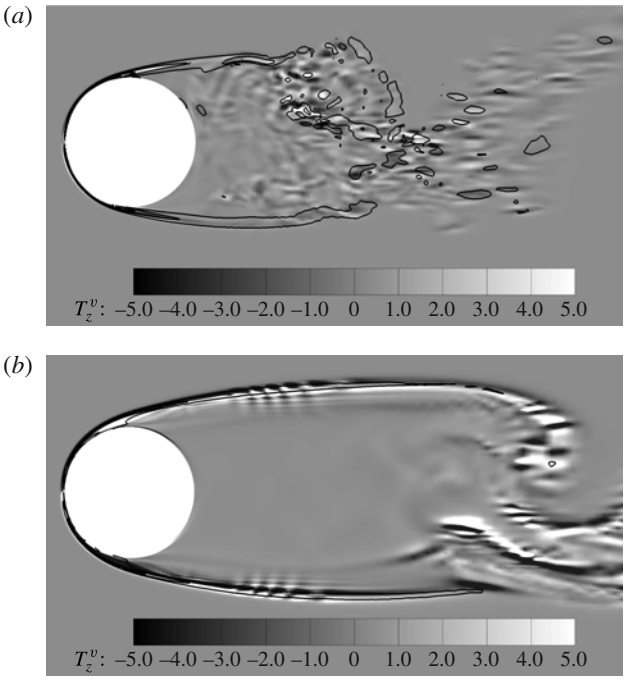

FIGURE 10. Contours of viscoelastic spanwise vorticity production, T_z^v, shown with the same scale for (*a*) $Wi = 10$, $L = 10$, $\beta = 0.9$; (*b*) $Wi = 10$, $L = 100$, $\beta = 0.9$. Solid lines show contours of spanwise vorticity ω_z at 10 levels ranging from $-70 \leqslant \omega_z \leqslant 70$.

effective at initiating the instability (see their figures 7 and 8). Kumar & Homsy (1999) confirmed this stabilization through two-dimensional nonlinear simulations and found that the viscoelastic sources and sinks of vorticity occur between primary rolls, which disrupts the streamwise distribution of vorticity and prevents the flow from effectively forming a single core. We therefore conclude that for the present case, as the layer tries to roll up and form the well-known 'cat eye' pattern, viscoelasticity responds by providing the vorticity source/sink pattern of figure 10(*b*) near the extensional regions between rolls, which perturbs the vorticity distribution in the streamwise direction and ultimately prevents the shear layer rollup. This source/sink pattern is therefore exactly out of phase with the location of the primary rolls (since it occurs in the region between cores), and for high enough L the shear layer remains completely intact and a primary vortex is shed nearly uninhibited.

Based on the definition of T_z^v, as the Weissenberg number is reduced (either that based on D or Wi_δ), one would expect that eventually, even at high L, rollup inhibition would no longer exist. Physically, this implies that viscoelastic stresses relax so quickly that they cannot produce a polymer torque large enough to inhibit rollup. Upon reducing the shear layer Weissenberg number to $Wi_\delta \approx 1$ (Wi based on D equal to 0.1), this is in fact observed. Figure 11 shows the same surface of spanwise vorticity seen in figure 8(*c*) for $L = 50$. It is clear that at such a low value of Wi_δ, the shear layer remains unstable despite the large value of L.

Based on the other regime identified by Kumar & Homsy (1999), one would also expect the inverse to be true: even at low L, large values of E_δ should be sufficient to stabilize the shear layer and prevent the rollup instability from forming. To test this,

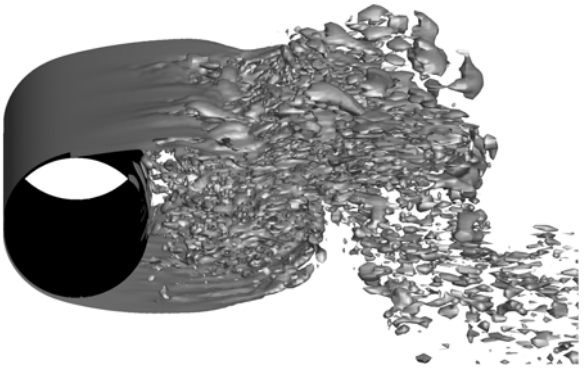

FIGURE 11. Instantaneous spanwise vorticity iso-surfaces ($\omega_z = \pm 9.0$) in $Re = 3900$ flow, for $Wi_\delta = 1$ ($Wi = 0.1$ based on D), $L = 50$, and $\beta = 0.9$. Low Wi_δ leads to polymer torques which are insufficient at stabilizing shear layer, even at $L = 50$.

FIGURE 12. Instantaneous spanwise vorticity iso-surfaces ($\omega_z = \pm 9.0$) in $Re = 3900$ flow, for $Wi_\delta = 2400$ ($Wi = 200$ based on D), $L = 10$, and $\beta = 0.9$. High Wi_δ does not further stabilize shear layer at $L = 10$ due to a saturation in viscoelastic stresses.

a simulation was performed with $L = 10$, while increasing the Weissenberg number to $Wi_\delta = 2400$ (Wi based on D of 200). This results in an elasticity number of $E_\delta \approx 5$ – an elasticity number seen by Kumar & Homsy (1999) to prevent rollup. The surface of spanwise vorticity for this case is displayed in figure 12, and should be compared with figure 8(*b*).

It is clear that despite a high elasticity number, and contrary to what is predicted by Kumar & Homsy (1999), increased elasticity numbers in the low L regime does not lead to a stabilized shear layer. The explanation for this apparent contradiction lies in the fact that the shear layers studied in Azaiez & Homsy (1994*a*) and Kumar & Homsy (1999) are developing; i.e. polymer stresses are forming at the same time rollup is initiated. Therefore, an increase in elasticity number results in a change in the vorticity diffusion coefficient relative to the polymer torque contribution. In the context of the cylinder wake, however, polymers are stretched to near 100 % of their extensibility upstream of the shear layer, leading to rollup formation in the presence of a saturated polymer stress state. Increasing Wi_δ implies that viscoelastic stresses are sustained for longer times, but in the region immediately behind the cylinder, these stresses are at a maximum for low L even for low values of E_δ. Therefore, increases in E_δ have no effect on the rollup instability which then forms.

	$\overline{p}_{min}$	$\lvert\overline{\omega}_z\rvert$
Newtonian	−1.11	8.81
$L = 10$	−1.04	8.74
$L = 50$	−0.721	5.33
$L = 100$	−0.571	5.506

TABLE 3. Comparison of instantaneous spanwise-average pressure $\bar{p}$ at a point during primary vortex rollup, as well as magnitude of spanwise vorticity at the point of minimum pressure. Viscoelastic cases are for $Wi = 10$ and $\beta = 0.9$.

6. Further discussion

It was mentioned in the Introduction that tip vortex cavitation suppression is one of the motivations behind studying high Reynolds number, viscoelastic bluff body flows. As one final note, it seems worthwhile to quickly relate the current study to this particular engineering application. For $Wi = 10$, increasing L was seen to greatly reduce the turbulence, not only in the shear layer but in the wake as well (cf. figure 6). We now look at the spanwise-averaged, minimum instantaneous pressures taken within a developing primary vortex core, which are presented in table 3. The minimum relative pressure inside a developing core is monotonically increasing (becoming less negative), indicating that polymer injection can greatly affect the point of cavitation inception for bluff body flows. Alongside the minimum pressure, table 3 also displays the spanwise vorticity magnitude at the point of minimum pressure. These values decrease monotonically as well, suggesting that rising core pressure is directly related to the reduction of vorticity within the developing vortex.

7. Conclusion

For the first time, simulations were performed of turbulent viscoelastic flow past a circular cylinder in order to study the effects which polymer additives have on the structure of a high Reynolds number wake. As in previous studies (Richter *et al.* 2010, 2011), the characteristic wake structure at $Re = 3900$, which begins with a transitioning detached shear layer, is stabilized in the presence of non-Newtonian elastic stresses. After the present analysis, we postulate that the mechanism of this stabilization is one where viscoelasticity stabilizes the shear layer through the development of vorticity sources and sinks within the layer, whose spatial orientation prevents Kelvin–Helmholtz rollup. This in turn allows for a coherent (as opposed to turbulent) primary vortex to be shed, which is then subject to the same types of elliptic and hyperbolic instabilities dominating the wake structure at Reynolds numbers below the onset of the Newtonian shear layer instabilities. This mechanism would explain the pattern found resembling that of the mode B instability seen in figure 6 at high polymer extensibility and, in addition to that found in Richter *et al.* (2011), constitutes another instance of wake stabilization due to viscoelasticity.

As a final point, it is noteworthy to briefly relate the underlying stabilization mechanisms observed in the present case with those of wall-bounded turbulent drag reduction. The key process observed in the high Reynolds number wake was the permanent suppression of the rollup instability in the detached shear layer due to a viscoelastic response in the region between forming rollers. The effects of polymer additives in turbulent wall-bounded flows is somewhat similar, in the sense that polymers act through stretching in the extensional regions between the vortical

structures, but the flow response to each is quite different. In the context of drag reduction, the process of polymer stretching between streamwise vortices extracts energy from the flow and reduces momentum transport to the wall, thus reducing the skin friction drag (Dubief *et al.* 2004), while for the cylinder wake viscoelasticity only needs to act in a localized region near the shear layer to allow a coherent primary vortex to form. Another important difference is the temporal behaviour of each process: in the cylinder wake, the rollup instability is permanently suppressed for high enough elasticity, while in the case of drag reduction the near-wall vortices are only temporarily weakened, and the effects of polymers are part of a turbulent self-regeneration cycle where the weakened vortices allow polymers to relax, which then results in turbulence starting once again (Xi & Graham 2010). Furthermore, another point of comparison lies in the cylinder boundary layer itself, which for our sub-critical Reynolds number remains laminar. At higher Reynolds numbers, the transition of this boundary layer will likely be directly affected by viscoelasticity, and mechanisms can be sought from the turbulent drag reduction literature. These points therefore highlight the importance of continued work to elucidate the unique roles which viscoelasticity plays in the bluff body wake.

Acknowledgements

The authors would like to acknowledge the Army High Performance Computing Research Center for Agility, Survivability and Informatics, Award No. W911NF-07-2-0027, High Performance Technologies Inc., and Department of the Army (Prime) for partial financial and computational support. In addition, this research has been funded in part by a KAUST research grant under the KAUST–Stanford Academic Excellence Alliance program. Any opinions, findings, and conclusions or recommendations expressed in this paper are those of the authors and do not necessarily reflect the views of the KAUST university. Finally, the authors acknowledge the following award for providing computing resources that have contributed to the research results reported within this paper: MRI-R2: Acquisition of a Hybrid CPU/GPU and Visualization Cluster for Multidisciplinary Studies in Transport Physics with Uncertainty Quantification. This award is funded under the American Recovery and Reinvestment Act of 2009 (Public Law 111-5).

REFERENCES

AZAIEZ, J. & HOMSY, G. 1994*a* Linear stability of free shear flow of viscoelastic liquids. *J. Fluid Mech.* **268**, 37–69.

AZAIEZ, J. & HOMSY, G. 1994*b* Numerical simulation of non-Newtonian free shear flows at high Reynolds numbers. *J. Non-Newtonian Fluid Mech.* **52**, 333–374.

BEAUDAN, P. & MOIN, P. 1994 Numerical experiments on the flow past a circular cylinder at sub-critical Reynolds number. *Tech. Rep.* TF-62. Stanford University, Stanford, CA, 94305.

BERGINS, C., NOWAK, M. & URBAN, M. 2001 The flow of a dilute cationic surfactant solution past a circular cylinder. *Exp. Fluids* **30**, 410–417.

BLOOR, M. S. 1964 The transition to turbulence in the wake of a circular cylinder. *J. Fluid Mech.* **19**, 290–304.

CADOT, O. & KUMAR, S. 2000 Experimental characterization of viscoelastic effects on two- and three-dimensional shear instabilities. *J. Fluid Mech.* **416**, 151–172.

CHAHINE, G. L., FREDERICK, G. F. & BATEMAN, R. D. 1993 Propeller tip vortex cavitation suppression using selective polymer injection. *J. Fluids Engng* **115**, 497–503.

COELHO, P. & PINHO, F. 2003*a* Vortex shedding in cylinder flow of shear-thinning fluids. Part I. Identification and demarcation of flow regimes. *J. Non-Newtonian Fluid Mech.* **110**, 143–176.

COELHO, P. & PINHO, F. 2003*b* Vortex shedding in cylinder flow of shear-thinning fluids. Part II. Flow characteristics. *J. Non-Newtonian Fluid Mech.* **110**, 177–193.

COELHO, P. M. & PINHO, F. T. 2004 Vortex shedding in cylinder flow of shear-thinning fluids. Part III. Pressure measurements. *J. Non-Newtonian Fluid Mech.* **121**, 55–68.

DIMITROPOULOS, C. D., DUBIEF, Y., SHAQFEH, E. S. G. & MOIN, P. 2006 Direct numerical simulation of polymer-induced drag reduction in turbulent boundary layer flow of inhomogeneous polymer solutions. *J. Fluid Mech.* **566**, 153–162.

DIMITROPOULOS, C., SURESHKUMAR, R. & BERIS, A. 1998 Direct numerical simulation of viscoelastic turbulent channel flow exhibiting drag reduction: effect of the variation of rheological parameters. *J. Non-Newtonian Fluid Mech.* **79**, 433–468.

DIMITROPOULOS, C., SURESHKUMAR, R., BERIS, A. & HANDLER, R. 2001 Budgets of Reynolds stress, kinetic energy and streamwise enstrophy in viscoelastic turbulent channel flow. *Phys. Fluids* **13** (4), 1016–1027.

DUBIEF, Y., TERRAPON, V. E., WHITE, C. M., SHAQFEH, E. S. G., MOIN, P. & LELE, S. K. 2005 New answers on the interaction between polymers and vortices in turbulent flows. *Flow Turbul. Combust.* **74** (4), 311–329.

DUBIEF, Y., WHITE, C. M., TERRAPON, V. E., SHAQFEH, E. S. G., MOIN, P. & LELE, S. K. 2004 On the coherent drag-reducing and turbulence-enhancing behaviour of polymers in wall flows. *J. Fluid Mech.* **514**, 271–280.

FRUMAN, D. H., PICHON, T. & CERRUTTI, P. 1995 Effect of a drag-reducing polymer solution ejection on tip vortex cavitation. *J. Mar. Sci. Technol.* **1**, 13–23.

HIBBERD, M., KWADE, M. & SCHARF, R. 1982 Influence of drag reducing additives on the structure of turbulence in a mixing layer. *Rheol. Acta* **21**, 582–586.

KATO, H. & MIZUNO, Y. 1983 An experimental investigation of viscoelastic flow past a circular cylinder. *Bull. Japan Soc. Mech. Engineers* **26** (214), 529–536.

KIM, K., LI, C., SURESHKUMAR, R., BALACHANDAR, S. & ADRIAN, R. 2007 Effects of polymer stresses on eddy structures in drag-reduced turbulent channel flow. *J. Fluid Mech.* **584**, 281–299.

KRAVCHENKO, A. 1998 B-spline methods and zonal grids for numerical simulations of turbulent flows. PhD thesis, Stanford University.

KRAVCHENKO, A. & MOIN, P. 2000 Numerical studies of flow over a circular cylinder at $Re_D = 3900$. *Phys. Fluids* **12** (2), 403–417.

KUMAR, S. & HOMSY, G. 1999 Direct numerical simulation of hydrodynamic instabilities in two- and three-dimensional viscoelastic free shear layers. *J. Non-Newtonian Fluid Mech.* **83**, 249–276.

MA, X., KARAMANOS, G. S. & KARNIADAKIS, G. E. 2000 Dynamics and low-dimensionality of a turbulent near wake. *J. Fluid Mech.* **410**, 29–65.

MA, X., SYMEONIDIS, V. & KARNIADAKIS, G. 2003 A spectral vanishing viscosity method for stabilizing viscoelastic flows. *J. Non-Newtonian Fluid Mech.* **115**, 125–155.

OGATA, S., OSANO, Y. & WATANABE, K. 2006 Effect of surfactant solutions on the drag and the flow pattern of a circular cylinder. *AIChE J.* **52** (1), 49–57.

ONG, L. & WALLACE, J. 1996 The velocity field of the turbulent very near wake of a circular cylinder. *Exp. Fluids* **20**, 441–453.

PARNAUDEAU, P., CARLIER, J., HEITZ, D. & LAMBALLAIS, E. 2008 Experimental and numerical studies of the flow over a circular cylinder at Reynolds number 3900. *Phys. Fluids* **20** (8), 1–14.

PRASAD, A. & WILLIAMSON, C. H. K. 1997 The instability of the shear layer separating from a bluff body. *J. Fluid Mech.* **333**, 375–402.

RAI, M. 2008 Towards direct numerical simulations of turbulent wakes. In *46th AIAA Aerospace Sciences Meeting and Exhibit. Paper* 2008-0544.

RAI, M. M. 2010 A computational investigation of the instability of the detached shear layers in the wake of a circular cylinder. *J. Fluid Mech.* **659**, 375–404.

RICHTER, D., IACCARINO, G. & SHAQFEH, E. S. G. 2010 Simulations of three-dimensional viscoelastic flows past a circular cylinder at moderate Reynolds numbers. *J. Fluid Mech.* **651**, 415–442.

RICHTER, D., SHAQFEH, E. S. G. & IACCARINO, G. 2011 Floquet stability analysis of viscoelastic flow over a cylinder. *J. Non-Newtonian Fluid Mech.* **166**, 554–565.

RIEDIGER, S. 1989 Influence of drag reducing additives on a plane mixing layer. In *Drag Reduction in Fluid Flows* (ed. R. H. J. Sellin & R. J. Moses), pp. 303–310. Ellis Horwood.

ROSHKO, A. 1954 On the development of turbulent wakes from vortex streets. NACA Report 1191.

SARPKAYA, T., RAINEY, P. & KELL, R. 1973 Flow of dilute polymer solutions about circular cylinders. *J. Fluid Mech.* **57**, 177–208.

SAUSSET, F., CADOT, O. & KUMAR, S. 2004 Experimental observation of frequency doubling in a viscoelastic mixing layer. *C. R. Mechanique* **332**, 1001–1006.

STONE, P., ROY, A., LARSON, R., WALEFFE, F. & GRAHAM, M. 2004 Polymer drag reduction in exact coherent structures of plane shear flow. *Phys. Fluids* **16** (9), 3470–3482.

SURESHKUMAR, R., BERIS, A. N. & HANDLER, R. A. 1997 Direct numerical simulation of the turbulent channel flow of a polymer solution. *Phys. Fluids* **9** (3), 743–755.

WILLIAMSON, C. H. K. 1996*a* Three-dimensional wake transition. *J. Fluid Mech.* **328**, 345–407.

WILLIAMSON, C. H. K. 1996*b* Vortex dynamics in the cylinder wake. *Annu. Rev. Fluid Mech.* **28**, 477–539.

XI, L. & GRAHAM, M. D. 2010 Active and hibernating turbulence in minimal channel flow of Newtonian and polymeric fluids. *Phys. Rev. Lett.* **104**, 218301.

YAKUSHIJI, R. 2009 Mechanism of tip vortex cavitation suppression. PhD thesis, University of Michigan.

YU, Z. & PHAN-THIEN, N. 2004 Three-dimensional roll-up of a viscoelastic mixing layer. *J. Fluid Mech.* **500**, 29–53.